GEOPHYSICS, VOL. 81, NO. 4 (JULY-AUGUST 2016); P. S207–S219, 11 FIGS.
10.1190/GEO2015-0487.1

CrossMark
click for updates

Downloaded 07/18/16 to 138.67.12.184. Redistribution subject to SEG license or copyright; see Terms of Use at http://library.seg.org/

Isotropic elastic wavefield imaging using the energy norm

Daniel Rocha[1], Nicolay Tanushev[2], and Paul Sava[1]

ABSTRACT

From the elastic-wave equation and the energy conservation principle, we have derived an energy norm that is applicable to imaging with elastic wavefields. Extending the concept of the norm to an inner product enables us to compare two related wavefields. For example, the inner product of source and receiver wavefields at each spatial location leads to an imaging condition. This new imaging condition outputs a single image representing the total reflection energy, and it contains individual terms related to the kinetic and potential energy (strain energy) from both extrapolated wavefields. An advantage of the proposed imaging condition compared with alternatives is that it does not suffer from polarity reversal at normal incidence, as do conventional images obtained using converted waves. Our imaging condition also accounted for the directionality of the wavefields in space and time. Based on this information, we have modified the imaging condition for attenuation of backscattering artifacts in elastic reverse time migration images. We performed numerical experiments that revealed the improved quality of the energy images compared with their conventional counterparts and the effectiveness of the imaging condition in attenuating backscattering artifacts even in media characterized by high spatial variability.

INTRODUCTION

Seismic wavefield imaging is usually implemented using the acoustic-wave equation because of the inaccurate assumption that only P-waves propagate in the subsurface. The search for more authentic images and subsurface information such as fracture distribution drives the development of wavefield imaging using the elastic-wave equation. Multicomponent seismic recording and improved computer resources have made elastic wavefield imaging possible (Denli and Huang, 2008; Yan and Sava, 2011; Yan and Xie, 2012; Chen and Huang, 2014; Duan and Sava, 2014a, 2014b).

For acoustic and elastic cases, wave-equation migration consists of two steps: (1) wavefield extrapolation in the subsurface using data recorded at the surface or the known source function and (2) the application of an imaging condition for the purpose of extracting the earth's reflectivity from wavefields (Claerbout, 1971; Dellinger and Etgen, 1990; Yan and Sava, 2009). If a two-way elastic-wave equation is used in the wavefield extrapolation step, followed by an imaging condition representing zero-lag crosscorrelation between the wavefields, the imaging procedure is called elastic reverse time migration (RTM) (Chang and McMechan, 1987; Hokstad et al., 1998). In recent years, many elastic imaging conditions have been proposed by exploiting the multicomponent aspect of the elastic wavefield and the possibility of decomposing the displacement fields into P- and S-wave modes (Etgen, 1988; Zhe and Greenhalg, 1997; Yan and Sava, 2007; Yan and Xie, 2010; Duan and Sava, 2014a). Correlating the displacement fields for each component of the source and receiver wavefields leads to images with a mixture of P- and S-wave modes, thus making interpretation challenging. In addition, the nine images generated by this kind of imaging condition represent another difficulty for 3D interpretation. Alternatively, if the displacement wavefields are separated into P- and S-waves using Helmholtz decomposition, one can correlate specific wave modes from source and receiver wavefields (Etgen, 1988; Yan and Sava, 2007). Another issue for displacement and potential imaging conditions is polarity reversal, which occurs in elastic images due to changes in the elastic wavefield polarization. Specifically, converted waves change sign due to the different orientation of P- and S-polarization vectors in relation to subsurface interfaces. For isotropic media, this polarity reversal occurs at normal incidence (Balch and Erdermir, 1994), which enables polarity reversal corrections either after angle-domain imaging (Yan and Sava, 2008) or by exploiting the relationship between incidence directions and reflector orientation (Duan and Sava, 2014a).

In addition to the issue of polarity reversal, elastic images have the disadvantage of containing artifacts that degrade image quality.

Manuscript received by the Editor 14 September 2015; revised manuscript received 11 January 2016; published online 30 May 2016.
[1]Center for Wave Phenomena, Colorado School of Mines, Golden, Colorado, USA. E-mail: drocha@mines.edu; psava@mines.edu.
[2]Z-Terra Inc., Houston, Texas, USA. E-mail: nicktan@z-terra.com.
© 2016 Society of Exploration Geophysicists. All rights reserved.

Downloaded 07/18/16 to 138.67.12.184. Redistribution subject to SEG license or copyright; see Terms of Use at http://library.seg.org/

As shown in detail elsewhere (Yan and Sava, 2007; Ravasi and Curtis, 2013; Duan and Sava, 2014a), injecting elastic data into a model (implementing back propagation) creates the so-called fake modes during the wavefield extrapolation step and leads to artifacts during the application of an imaging condition. These artifacts might be present even after stacking, masking weak reflections in the final image (Duan and Sava, 2014b). A second type of artifact appears if the elastic model contains sharp interfaces. In this case, backscattered reflections occur during the wavefield extrapolation step, and the application of conventional imaging conditions create low-wavenumber artifacts in the image (Youn and Zhou, 2001; Yoon and Marfurt, 2006; Guitton et al., 2007; Denli and Huang, 2008; Chen and Huang, 2014). Here, we address the second type of artifact; the first type is beyond the scope of this paper because it requires nonconventional data acquisition or additional assumptions.

Considering the issue of polarity reversal and backscattering artifacts, and the fact that several images for different wave modes are difficult to interpret, we seek an imaging condition that outputs an attribute of the earth's reflectivity into a single image. This single image should facilitate interpretation and provide a concise description of the imaged structures. In addition, we intend to assign a clear physical explanation to images obtained with this imaging condition.

We propose a new imaging condition that captures all wave modes into a single image, with attenuated backscattering artifacts and without polarity reversal at normal incidence. Our imaging condition is derived from the energy conservation principle of an elastic wavefield.

THEORY

We use energy conservation laws analogous to the acoustic case (Rocha et al., 2015) to derive a function that measures the energy of a wavefield. This energy function also enables us to form an imaging condition for two extrapolated elastic wavefields from source and receivers.

Wavefield extrapolation

For an isotropic medium enclosed by a domain $\Omega \subset \mathbb{R}^3$, we can write a wave equation for the displacement vector with no external sources (Aki and Richards, 2002):

$$\rho\ddot{\mathbf{U}} = \nabla[\lambda(\nabla\cdot\mathbf{U})] + \nabla[\mu\cdot(\nabla\mathbf{U}+\nabla\mathbf{U}^{\mathrm{T}})]. \tag{1}$$

In equation 1, the elastic wavefield is a function of space $\mathbf{x}$, time t, and experiment index e: $\mathbf{U}(e,\mathbf{x},t)$ for $\mathbf{x}\in\Omega$ and $t\in[0,T]$. The dot symbol indicates dot product, the superscript dot indicates the first time differentiation, and the double dot indicates the second time differentiation. Because elastic waves propagate at a finite speed, we can take the spatial domain Ω large enough, and then assume homogeneous boundary conditions for $\mathbf{U}$ and its derivatives, which means that $\mathbf{U}$ and its derivatives vanish on the boundary of Ω ($\partial\Omega$) for all $t\in[0,T]$. The density and the Lamé parameters are functions of space $\rho(\mathbf{x})$, $\lambda(\mathbf{x})$, and $\mu(\mathbf{x})$, and we assume these parameters vary slowly in Ω, which allows us to neglect their spatial derivatives, thus leading to a different wave equation:

$$\rho\ddot{\mathbf{U}} = \lambda[\nabla(\nabla\cdot\mathbf{U})] + \mu[\nabla\cdot(\nabla\mathbf{U}+\nabla\mathbf{U}^{\mathrm{T}})], \tag{2}$$

and equation 2 can be used to extrapolate elastic wavefield for arbitrary sources, assuming that we know the spatial distribution of parameters ρ, λ, and μ.

Elastic wavefield energy

The total energy of an acoustic wavefield is conserved; i.e., we can write (Appendix A)

$$\dot{E}(t) = \int_\Omega \dot{U}(\ddot{U} - c^2\nabla^2 U)d\mathbf{x} = 0. \tag{3}$$

We develop the energy conservation expression for elastic wavefields analogously by multiplying the time derivative of the displacement wavefield (i.e., particle velocity) with the corresponding wave equation, followed by integration over the whole physical domain Ω. If we apply the dot product between the wave equation in equation 2 and $\dot{\mathbf{U}}$, we obtain

$$\rho\dot{\mathbf{U}}\cdot\ddot{\mathbf{U}} = \lambda[\dot{\mathbf{U}}\cdot[\nabla(\nabla\cdot\mathbf{U})]] + \mu[\dot{\mathbf{U}}\cdot[\nabla\cdot(\nabla\mathbf{U}+\nabla\mathbf{U}^{\mathrm{T}})]]. \tag{4}$$

Rearranging the term on the left side by the chain rule leads to

$$\frac{1}{2}\frac{\partial}{\partial t}\rho|\dot{\mathbf{U}}|^2 = \lambda[\dot{\mathbf{U}}\cdot[\nabla(\nabla\cdot\mathbf{U})]] + \mu[\dot{\mathbf{U}}\cdot[\nabla\cdot(\nabla\mathbf{U}+\nabla\mathbf{U}^{\mathrm{T}})]], \tag{5}$$

and integrating over the whole domain, we obtain

$$\frac{1}{2}\frac{\partial}{\partial t}\int_\Omega \rho|\dot{\mathbf{U}}|^2 d\mathbf{x} = \int_\Omega \lambda[\dot{\mathbf{U}}\cdot[\nabla(\nabla\cdot\mathbf{U})]]d\mathbf{x} + \int_\Omega \mu[\dot{\mathbf{U}}\cdot[\nabla\cdot(\nabla\mathbf{U}+\nabla\mathbf{U}^{\mathrm{T}})]]d\mathbf{x}. \tag{6}$$

We can develop the two terms on the right side of equation 6 separately. For the first term, using integration by parts, we obtain

$$\int_\Omega \lambda[\dot{\mathbf{U}}\cdot[\nabla(\nabla\cdot\mathbf{U})]]d\mathbf{x} = \int_\Omega \lambda[\nabla\cdot[\dot{\mathbf{U}}(\nabla\cdot\mathbf{U})]]d\mathbf{x} - \int_\Omega \lambda(\nabla\cdot\dot{\mathbf{U}})(\nabla\cdot\mathbf{U})d\mathbf{x}. \tag{7}$$

The first term on the right side of equation 7 can be turned into a surface integral by the Divergence Theorem (Boas, 2006), thus becoming zero; the wavefield $\mathbf{U}$ and its derivatives vanish on the boundary $\partial\Omega$, as explained in the preceding section

$$\int_\Omega \lambda[\nabla\cdot[\dot{\mathbf{U}}(\nabla\cdot\mathbf{U})]]d\mathbf{x} = \int_{\partial\Omega} \lambda[\dot{\mathbf{U}}(\nabla\cdot\mathbf{U})]\cdot\mathbf{n}d\mathbf{x} = 0. \tag{8}$$

Therefore, equation 7 becomes

$$\int_\Omega \lambda[\dot{\mathbf{U}}\cdot[\nabla(\nabla\cdot\mathbf{U})]]d\mathbf{x} = -\int_\Omega \lambda(\nabla\cdot\dot{\mathbf{U}})(\nabla\cdot\mathbf{U})d\mathbf{x}. \tag{9}$$

Using the chain rule, we arrange the term on the right side as follows:

Downloaded 07/18/16 to 138.67.12.184. Redistribution subject to SEG license or copyright; see Terms of Use at http://library.seg.org/

$$\int_\Omega \lambda(\nabla\cdot\dot{\mathbf{U}})(\nabla\cdot\mathbf{U})d\mathbf{x} = \frac{1}{2}\frac{\partial}{\partial t}\int_\Omega \lambda|\nabla\cdot\mathbf{U}|^2 d\mathbf{x}. \quad (10)$$

Similarly, for the second term on the right side of equation 6, we use integration by parts:

$$\begin{aligned}\int_\Omega \mu[\dot{\mathbf{U}}\cdot[\nabla\cdot(\nabla\mathbf{U}+\nabla\mathbf{U}^{\mathrm{T}})]]d\mathbf{x}&\\ = \int_\Omega \mu[\nabla\cdot[\dot{\mathbf{U}}\cdot(\nabla\mathbf{U}+\nabla\mathbf{U}^{\mathrm{T}})]]d\mathbf{x}&\\ - \int_\Omega \mu(\nabla\dot{\mathbf{U}}):(\nabla\mathbf{U}+\nabla\mathbf{U}^{\mathrm{T}})d\mathbf{x},&\end{aligned} \quad (11)$$

where the symbol : indicates the Frobenius product between two matrices (Appendix B). The first integral of the right side goes to zero by the divergence theorem; therefore, we can write

$$\begin{aligned}\int_\Omega \mu[\dot{\mathbf{U}}\cdot[\nabla\cdot(\nabla\mathbf{U}+\nabla\mathbf{U}^{\mathrm{T}})]]d\mathbf{x}&\\ = -\int_\Omega \mu(\nabla\dot{\mathbf{U}}):(\nabla\mathbf{U}+\nabla\mathbf{U}^{\mathrm{T}})d\mathbf{x}.&\end{aligned} \quad (12)$$

Developing further, using the properties of the Frobenius product, we obtain

$$\begin{aligned}-\int_\Omega \mu(\nabla\cdot\dot{\mathbf{U}}):(\nabla\mathbf{U}+\nabla\mathbf{U}^{\mathrm{T}})d\mathbf{x} &= \\ = -\int_\Omega \mu\mathrm{Tr}[\nabla\dot{\mathbf{U}}(\nabla\mathbf{U}^{\mathrm{T}}+\nabla\mathbf{U})]d\mathbf{x},&\\ = -\int_\Omega \mu\mathrm{Tr}[\nabla\dot{\mathbf{U}}\nabla\mathbf{U}^{\mathrm{T}}+\nabla\dot{\mathbf{U}}\nabla\mathbf{U}]d\mathbf{x},&\\ = -\frac{1}{2}\frac{\partial}{\partial t}\int_\Omega \mu\mathrm{Tr}[\nabla\mathbf{U}\nabla\mathbf{U}^{\mathrm{T}}+\nabla\mathbf{U}\nabla\mathbf{U}]d\mathbf{x},&\\ = -\frac{1}{2}\frac{\partial}{\partial t}\int_\Omega \mu[\nabla\mathbf{U}:\nabla\mathbf{U}+\nabla\mathbf{U}:\nabla\mathbf{U}^{\mathrm{T}}]d\mathbf{x}.&\end{aligned} \quad (13)$$

Rewriting equation 6 with the new right side terms from equations 10 and 13 leads to

$$\frac{1}{2}\frac{\partial}{\partial t}\int_\Omega \rho\|\dot{\mathbf{U}}\|^2+\lambda\|\nabla\cdot\mathbf{U}\|^2+\mu[\nabla\mathbf{U}:\nabla\mathbf{U}+\nabla\mathbf{U}:\nabla\mathbf{U}^{\mathrm{T}}]d\mathbf{x}=0, \quad (14)$$

and we obtain an expression in the form $\dot{E}(t)=0$, which is the mathematical formulation of the conservation of energy over time. Therefore, the function

$$\begin{aligned}E(t) = \frac{1}{2}\int_\Omega \rho\|\dot{\mathbf{U}}\|^2+\lambda\|\nabla\cdot\mathbf{U}\|^2&\\ +\mu[\nabla\mathbf{U}:\nabla\mathbf{U}+\nabla\mathbf{U}:\nabla\mathbf{U}^{\mathrm{T}}]d\mathbf{x}&\end{aligned} \quad (15)$$

measures the total energy of the wavefield within a domain.

Physical interpretation

Equation 15 can be treated as a special case of the total energy of a wavefield in an anisotropic medium:

$$E(t) = \frac{1}{2}\int_\Omega \rho\|\dot{\mathbf{U}}\|^2+\underline{\underline{\mathbf{c}}}\,\underline{\mathbf{e}}:\underline{\mathbf{e}}d\mathbf{x}, \quad (16)$$

where $\underline{\underline{\mathbf{c}}}$ is the fourth-rank stiffness tensor and $\underline{\mathbf{e}}=1/2(\nabla\mathbf{U}+\nabla\mathbf{U}^{\mathrm{T}})$ is the strain tensor. The first term in the integrand of equation 16 represents the kinetic energy of the wavefield, and the second term is the strain energy that represents the potential energy of the wavefield. Substituting the stiffness coefficients for the isotropic case in equation 16, we obtain equation 15 (Appendix C). Therefore, the second and third terms in equation 15 are equal to the strain energy function for isotropic media. Due to the fact that the wavefield vanishes at $\partial\Omega$, the total energy in equation 15 can be simplified further, considering that the second-order spatial derivatives of the wavefield are continuous (Appendix D):

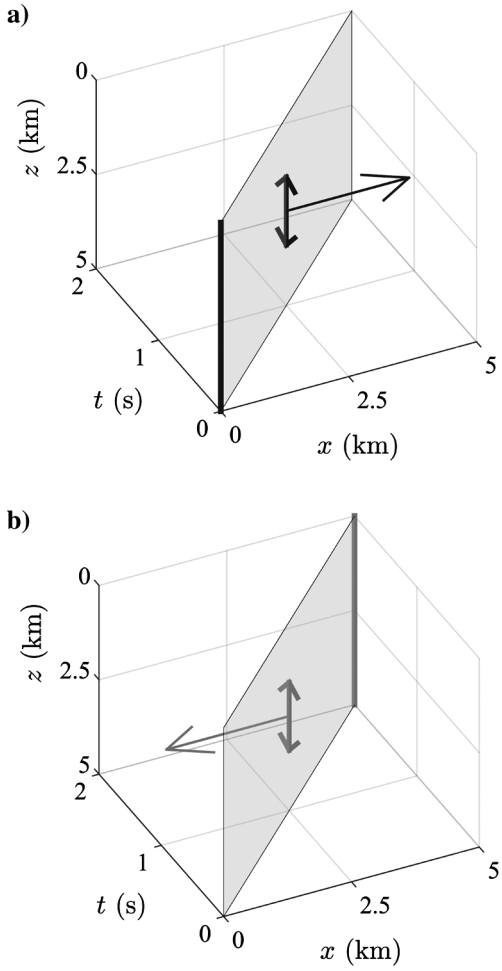


Figure 1. Schematic plots showing the evolution of elastic plane-wave wavefields over time, originated by (a) a vertical source at $x=0$ km and (b) a vertical receiver line at $x=5$ km. Notice that (b) represents a wavefield propagating backward in time. The thick arrows represent pure S-wave polarization, and the thin arrows represent the slowness vectors.

$$E(t) = \frac{1}{2}\int_{\Omega} \rho \|\dot{\mathbf{U}}\|^2 + (\lambda+\mu)\|\nabla\cdot\mathbf{U}\|^2 + \mu\nabla\mathbf{U}:\nabla\mathbf{U}d\mathbf{x}. \quad (17)$$

It is important to note that the total energy derivation depends on the wave equation used in the first place. Equation 17 could also be derived starting from the following wave equation:

$$\rho\ddot{\mathbf{U}} = (\lambda+\mu)\nabla(\nabla\cdot\mathbf{U}) + \mu\nabla^2\mathbf{U}, \quad (18)$$

which is equivalent to equation 2 if the second-order spatial derivatives of the wavefield are continuous (Appendix E).

Imaging condition

Considering two wavefields $\mathbf{U}$ and $\mathbf{V}$, and the elastic energy norm in equation 17, we define the following inner product:

$$\langle \mathbf{U}, \mathbf{V}\rangle_E = \int_0^T \int_{\Omega} \rho\dot{\mathbf{U}}\cdot\dot{\mathbf{V}} + (\lambda+\mu)(\nabla\cdot\mathbf{U})(\nabla\cdot\mathbf{V}) + \mu\nabla\mathbf{U}:\nabla\mathbf{V}d\mathbf{x}. \quad (19)$$

We propose a new elastic imaging condition based on the inner product in equation 19 between the source and receiver wavefields, followed by integration over time and experiments:

$$I_E = \sum_{e,t}[\rho\dot{\mathbf{U}}\cdot\dot{\mathbf{V}} + (\lambda+\mu)(\nabla\cdot\mathbf{U})(\nabla\cdot\mathbf{V}) + \mu(\nabla\mathbf{U}):(\nabla\mathbf{V})], \quad (20)$$

where $\mathbf{U}(e,\mathbf{x},t)$ and $\mathbf{V}(e,\mathbf{x},t)$ are the source and receiver vector wavefields, respectively, and $I_E(\mathbf{x})$ is a scalar image obtained based

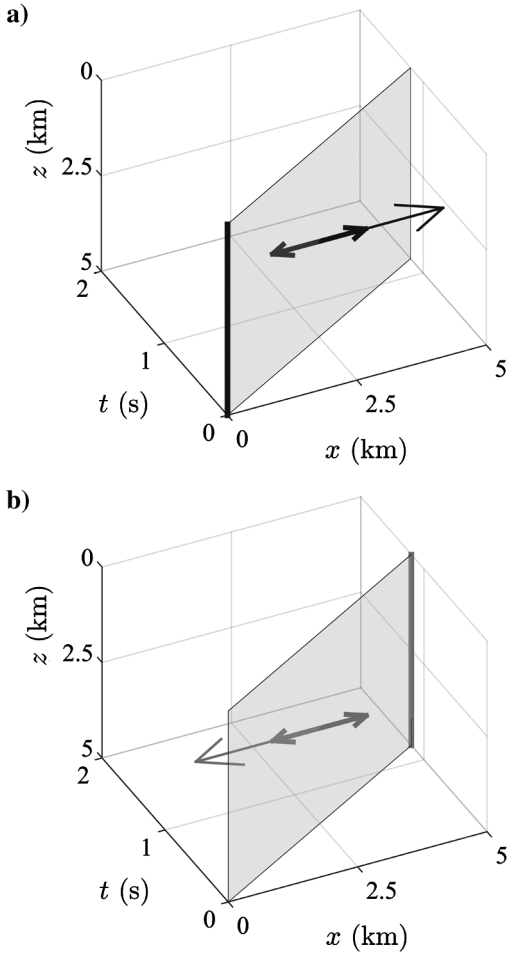


Figure 2. Schematic plots showing the evolution of elastic plane-wave wavefields over time, originated by (a) a vertical source at $x = 0$ km and (b) a vertical receiver line at $x = 5$ km. Notice that (b) represents a wavefield propagating backward in time. The thick arrows represent pure P-wave polarization, and the thin arrows represent the slowness vectors. Note that the wavefields propagate faster than the ones in figure 0 because P-wave velocity is faster than the S-wave velocity.

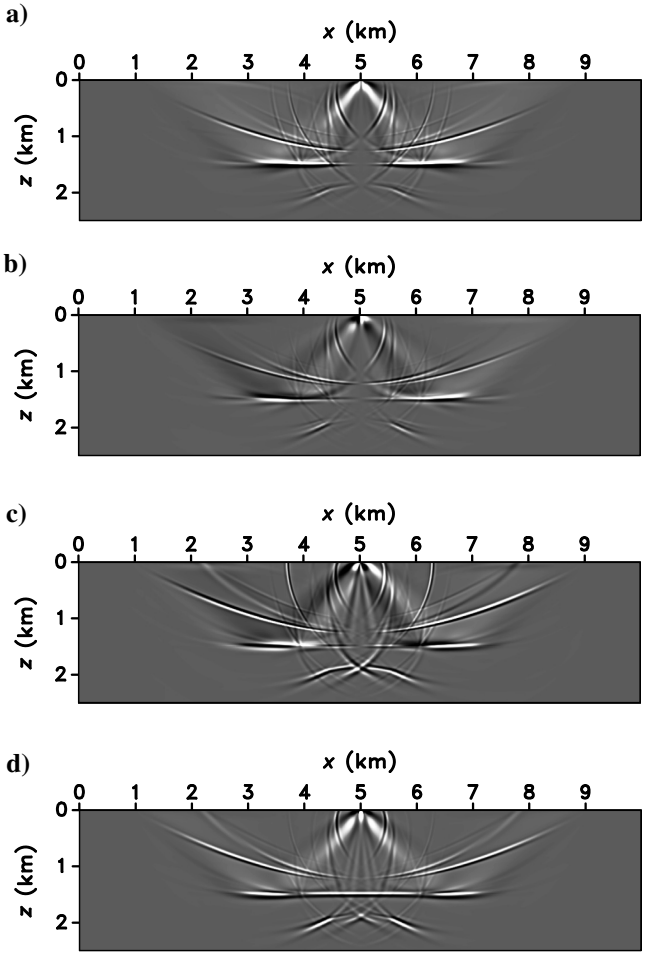


Figure 3. Imaging conditions using displacement components for a horizontal reflector with a vertical displacement source at $x = 5$ km: (a) U_xV_x, (b) U_xV_z, (c) U_zV_x, and (d) U_zV_z image, where $\{U_x, U_z\}$ and $\{V_x, V_z\}$ are the horizontal and vertical components of the source and receiver wavefields, respectively. The type of artifacts that are present in all images occur due to the fake modes, which are generated when injecting an incomplete displacement field in the receiver wavefield. Polarity reversal at normal incidence occurs for (b and c). The reflector is present in the migration velocity to generate backscattering artifacts, which are visible in all images.

Downloaded 07/18/16 to 138.67.12.184. Redistribution subject to SEG license or copyright; see Terms of Use at http://library.seg.org/

Downloaded 07/18/16 to 138.67.12.184. Redistribution subject to SEG license or copyright; see Terms of Use at http://library.seg.org/

on the elastic wavefields. We can describe this imaging condition as a dot product between the following multidimensional vectors:

$$\square\mathbf{U} = \left\{\sqrt{\rho}\dot{\mathbf{U}}, \sqrt{\lambda+\mu}(\nabla\cdot\mathbf{U}), \sqrt{\mu}(\nabla\mathbf{U})\right\}, \tag{21}$$

$$\square\mathbf{V} = \left\{\sqrt{\rho}\dot{\mathbf{V}}, \sqrt{\lambda+\mu}(\nabla\cdot\mathbf{V}), \sqrt{\mu}(\nabla\mathbf{V})\right\}, \tag{22}$$

where equations 21 and 22 define multidimensional vectors with 13 components in which three components are the wavefield time derivatives, $\dot{\mathbf{U}}$ and $\dot{\mathbf{V}}$, one is the scaled divergence of the wavefields, $\nabla\cdot\mathbf{U}$ and $\nabla\cdot\mathbf{V}$, and nine are from the displacement gradients, $\nabla\mathbf{U}$ and $\nabla\mathbf{V}$.

Therefore, we can rewrite equation 20 as

$$I_E = \sum_{e,t}\square\mathbf{U}\cdot\square\mathbf{V}. \tag{23}$$

This expression is analogous to the similar imaging condition developed for acoustic wavefields (Rocha et al., 2015), and has similar physical interpretation and application, as discussed in the next section.

Backscattering attenuation

Vectors $\square\mathbf{U}$ and $\square\mathbf{V}$ are related to the polarization and propagation direction of the elastic wavefields $\mathbf{U}$ and $\mathbf{V}$. Decomposing the wavefield $\mathbf{U}$ in plane waves, we obtain

$$\mathbf{U} = \mathbf{u}_0 e^{i\omega(\mathbf{p}\cdot\mathbf{x}-t)}, \tag{24}$$

where $\mathbf{u}_0$ is the polarization vector, $\mathbf{p}$ is the slowness vector, and ω is the frequency. We assume that ω is large and that the vectors $\mathbf{u}_0$ and $\mathbf{p}$ are slowly varying in space and time, which makes the spatial and temporal derivatives of $\mathbf{u}_0$ and $\mathbf{p}$ small compared to ω. Substituting the plane wave definition in equation 24 as trial solution of the elastic equation in equation 18, we obtain an expression that is equiv-

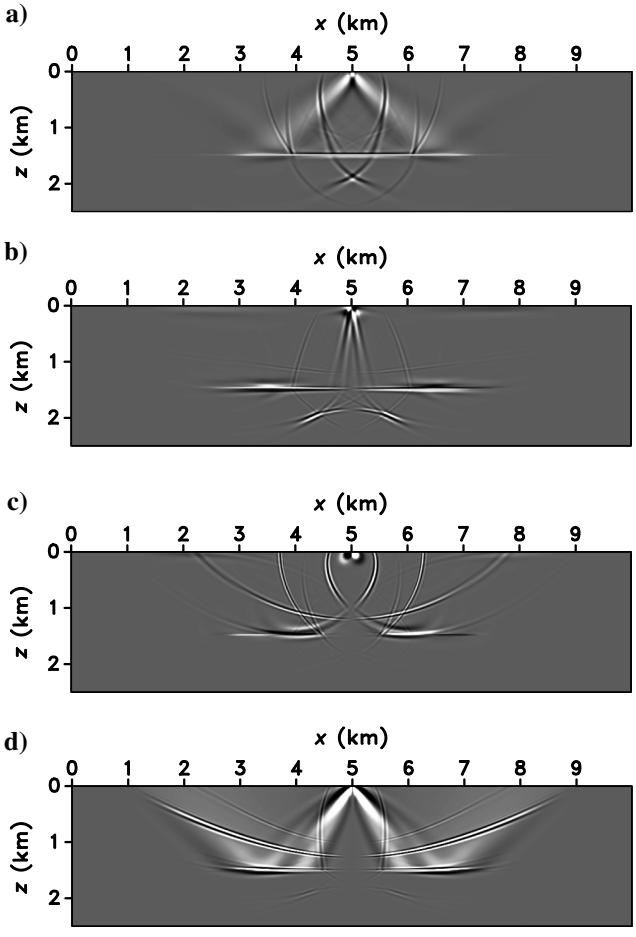


Figure 4. Imaging conditions using potentials for a horizontal reflector with a vertical displacement source at $x = 5$ km: (a) PP, (b) PS, (c) SP, and (d) SS image. Fake modes artifacts are also present in these images, analogously to Figure 2. The presence of a velocity contrast and the correlation between same wave modes in (a and d) generates backscattering artifacts, and the correlation between different wave modes in (b and c) generates polarity reversal at normal incidence.

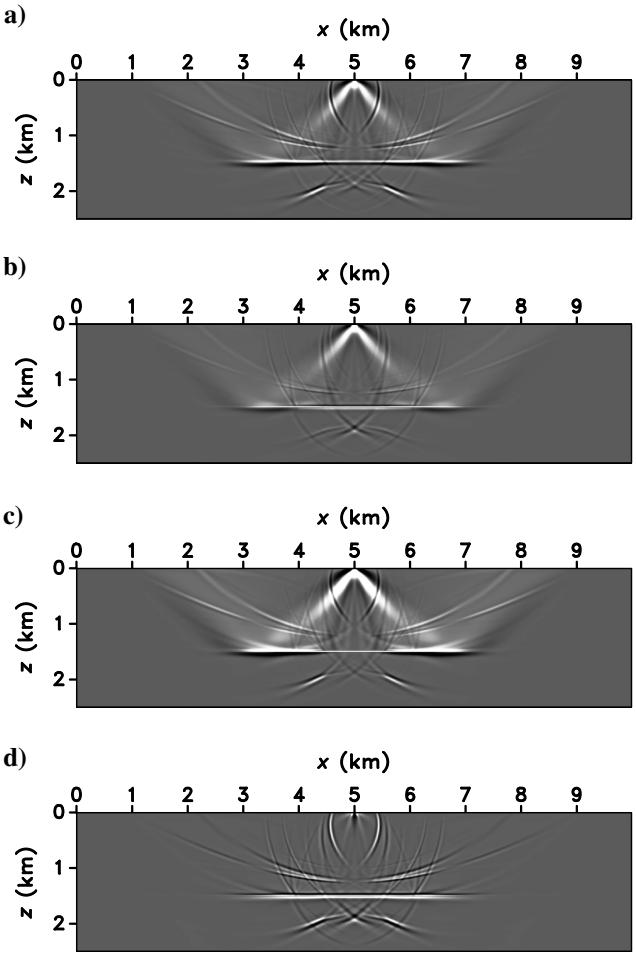


Figure 5. Individual terms of the energy imaging condition for a horizontal reflector present in the migration velocity, and a vertical displacement source at $x = 5$ km: (a) kinetic energy, (b) strain energy, (c) total energy, and (d) the imaging condition in equation 35. Compared with images from Figures 2–4, (d) is the only image with attenuated backscattering artifacts and without polarity reversal at normal incidence.

alent to the Christoffel equation when reduced to isotropic media (Appendix F),

$$\rho \mathbf{u}_0 = (\lambda + \mu)(\mathbf{u}_0 \cdot \mathbf{p})\mathbf{p} + \mu(\mathbf{p} \cdot \mathbf{p})\mathbf{u}_0. \tag{25}$$

Taking the dot product of equation 25 by $\mathbf{u}_0$ leads to

$$\rho|\mathbf{u}_0|^2 = (\lambda + \mu)(\mathbf{u}_0 \cdot \mathbf{p})^2 + \mu|\mathbf{p}|^2|\mathbf{u}_0|^2. \tag{26}$$

The terms in equation 26 are present in the definition of $\Box\mathbf{U}$, stated in equation 21:

$$\dot{\mathbf{U}} = -i\omega\mathbf{u}_0 e^{i\omega(\mathbf{p}\cdot\mathbf{x}-t)}, \tag{27}$$

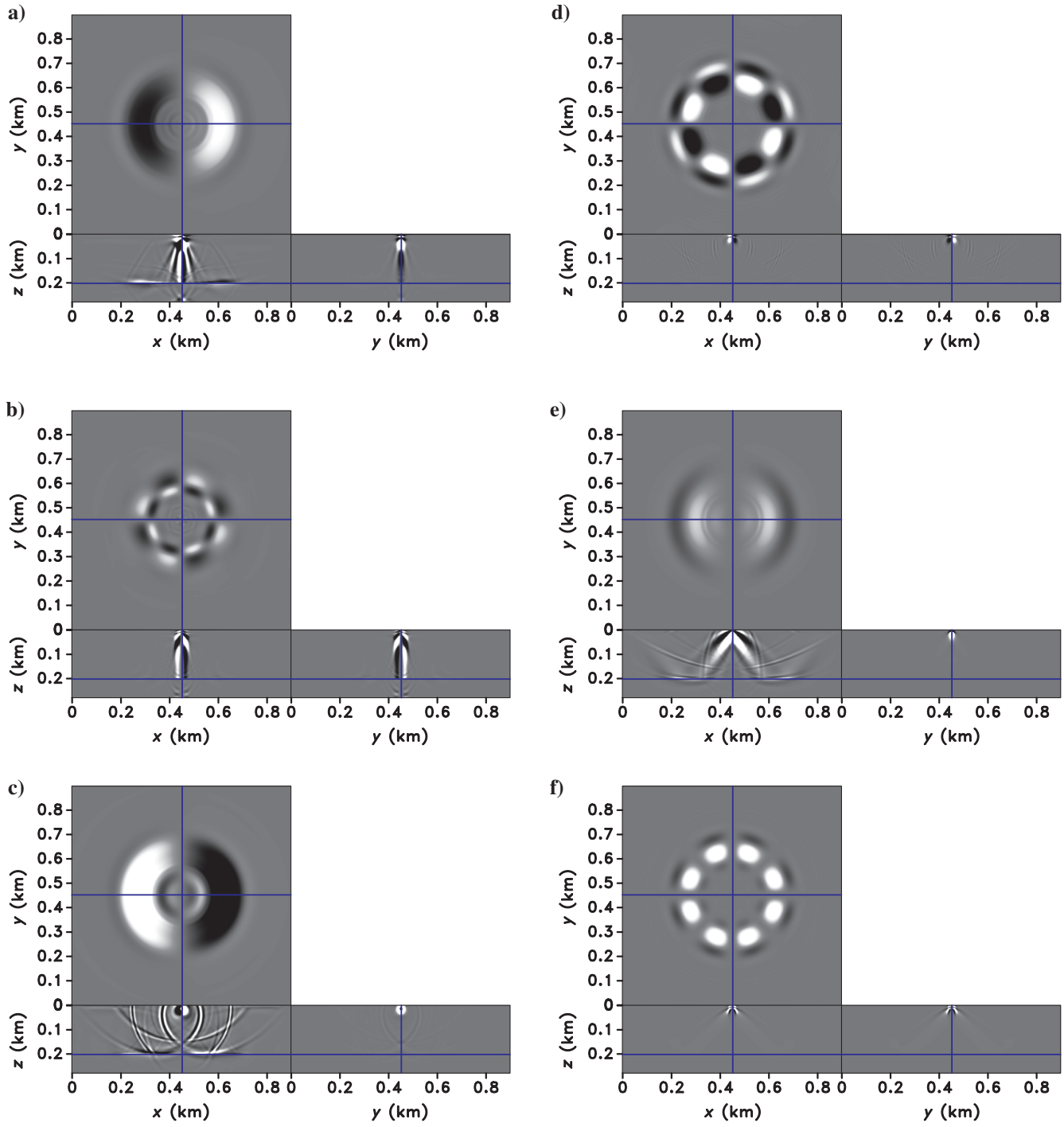


Figure 6. Images using conventional imaging conditions for a 3D elastic experiment with a horizontal reflector located at $z = 0.2$ km: (a) PS_y, (b) PS_z, (c) S_yP (d) S_zP, (e) S_yS_y, and (f) S_zS_z images. For images using correlation between the same wave modes, backscattering artifacts exist in (e and f); for the other images that use correlation between different wave modes, polarity reversal occurs at normal incidence.

Downloaded 07/18/16 to 138.67.12.184. Redistribution subject to SEG license or copyright; see Terms of Use at http://library.seg.org/

$$\nabla \cdot \mathbf{U} = i\omega(\mathbf{u}_0 \cdot \mathbf{p})e^{i\omega(\mathbf{p}\cdot\mathbf{x}-t)}, \tag{28}$$

$$\nabla\mathbf{U} = i\omega(\mathbf{u}_0 \otimes \mathbf{p})e^{i\omega(\mathbf{p}\cdot\mathbf{x}-t)}, \tag{29}$$

where the symbol $\otimes$ indicates the outer product between two vectors, resulting in a matrix. Therefore, the dot product of $\Box\mathbf{U}$ with itself is

$$\begin{aligned}\Box\mathbf{U}\cdot\Box\mathbf{U} &= \rho\ddot{\mathbf{U}}^*\cdot\ddot{\mathbf{U}} + (\lambda+\mu)(\nabla\cdot\mathbf{U}^*)(\nabla\cdot\mathbf{U}) \\ &\quad + \mu(\nabla\mathbf{U}^*):(\nabla\mathbf{U}) \\ &= -\omega^2[\rho|\mathbf{u}_0|^2 + (\lambda+\mu)(\mathbf{u}_0\cdot\mathbf{p})^2 + \mu|\mathbf{p}|^2|\mathbf{u}_0|^2],\end{aligned} \tag{30}$$

where $*$ indicates complex conjugate. We seek to define an imaging condition that attenuates waves of the source and receiver wavefields propagating along the same path and with the same polarization, i.e., elastic backscattering. Defining $(\Box\mathbf{V})^\dagger$ as

$$(\Box\mathbf{V})^\dagger = \left\{-\sqrt{\rho}\ddot{\mathbf{V}}, \sqrt{\lambda+\mu}(\nabla\cdot\mathbf{V}), \sqrt{\mu}(\nabla\mathbf{V})\right\}, \tag{31}$$

we can compute the dot product between $\Box\mathbf{U}$ and $(\Box\mathbf{V})^\dagger$ as

$$\begin{aligned}\Box\mathbf{U}\cdot(\Box\mathbf{V})^\dagger &= -\rho\ddot{\mathbf{U}}^*\cdot\ddot{\mathbf{V}} + (\lambda+\mu)(\nabla\cdot\mathbf{U}^*)(\nabla\cdot\mathbf{V}) \\ &\quad + \mu(\nabla\mathbf{U}^*):(\nabla\mathbf{V}).\end{aligned} \tag{32}$$

In case $\mathbf{U}$ and $\mathbf{V}$ share the same polarization $\mathbf{u}_0$ and slowness vector $\mathbf{p}$, equation 32 becomes

$$\Box\mathbf{U}\cdot(\Box\mathbf{V})^\dagger = \omega^2[\rho|\mathbf{u}_0|^2 - (\lambda+\mu)(\mathbf{u}_0\cdot\mathbf{p})^2 - \mu|\mathbf{p}|^2|\mathbf{u}_0|^2]. \tag{33}$$

Using the relation in equation 26, we obtain the following for equation 33:

$$\Box\mathbf{U}\cdot(\Box\mathbf{V})^\dagger = 0, \tag{34}$$

i.e., the dot product is zero everywhere except at locations where reflectors exist or different wave modes interact because the vectors $\mathbf{p}$ and $\mathbf{u}_0$ are different for $\mathbf{U}$ and $\mathbf{V}$ at these locations. Therefore, the dot product in equation 32 suppresses the events that propagate on the same path and have the same polarization. Such events include reflection backscattering, diving, direct, and head waves from the same wave modes. Therefore, the imaging condition

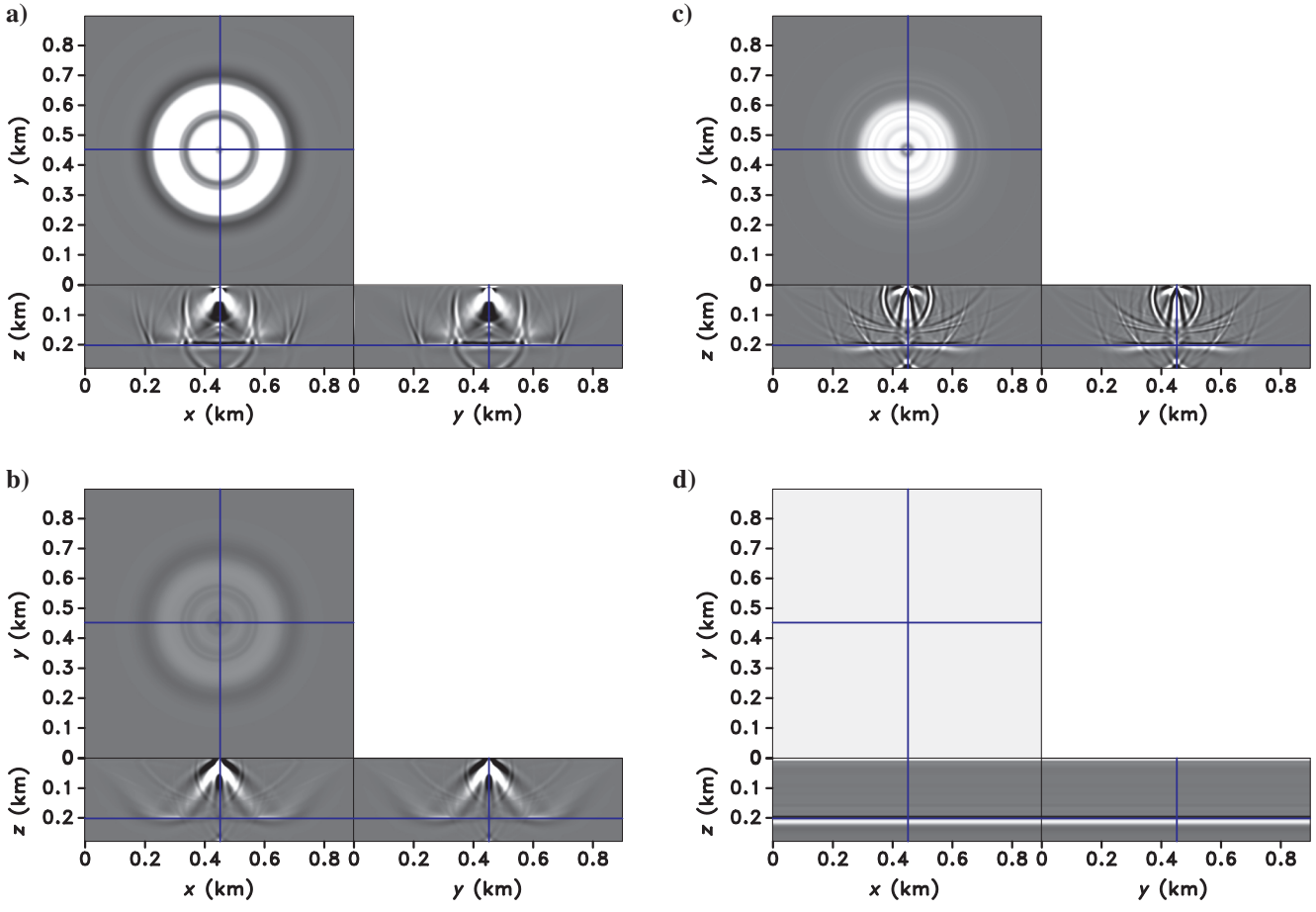


Figure 7. (a) PP image and images using energy imaging conditions for a 3D elastic experiment with a horizontal reflector located at $z = 0.2$ km, (b) total energy imaging condition, and (c) imaging condition from equation 35. Although (c) still has fake mode artifacts, stacking over shots attenuates this artifacts, as shown in (d), which is a stacked version of (c) using shots at every point at the surface.

Downloaded 07/18/16 to 138.67.12.184. Redistribution subject to SEG license or copyright; see Terms of Use at http://library.seg.org/

$$I_E^{\dagger} = \sum_{e,t} \square\mathbf{U} \cdot (\square\mathbf{V})^{\dagger} \tag{35}$$

attenuates backscattering artifacts in elastic RTM images. This imaging condition, with respect to the one in equation 23, has a minus sign applied to the time derivative component of $\square\mathbf{V}$ (defined in equation 31).

Due to the multidimensional character of $\square\mathbf{U}$ and $(\square\mathbf{V})^{\dagger}$, which have 13 components, it is difficult to visualize the orthogonality of these vectors in the imaging condition shown in equation 35 for the most general case possible. However, we can illustrate this idea by simple schematic examples.

Figures 1 and 2 show schematic plots describing imaging experiments using plane waves with S and P pure polarizations. Figures 1a and 2a describe the evolution of the source wavefields for S- and P-wave modes, with plane wave sources located at $x = 0$ km. Extrapolating the data backward in time from the vertical line of receivers at $x = 5$ km generates receiver wavefields for S- and P-wave modes shown in Figures 1b and 2b, respectively. In Figures 1 and 2, the thick arrows represent the directions of polarization and the thin arrows represent the slowness vectors. The vectors $\square\mathbf{U}$ and $(\square\mathbf{V})^{\dagger}$ for the S-wave experiment in Figure 1 are obtained using the definitions in equations 21 and 31, $\mathbf{u}_0 = \{0, 0, 1\}$ and $\mathbf{p} = \{\sqrt{(\rho/\mu)}, 0, 0\}$,

$$\square\mathbf{U} = i\omega\sqrt{\rho}\{-1,0,1\}e^{i\omega(\mathbf{p}\cdot\mathbf{x}-t)}, \tag{36}$$

$$(\square\mathbf{V})^{\dagger} = i\omega\sqrt{\rho}\{1,0,1\}e^{i\omega(\mathbf{p}\cdot\mathbf{x}-t)}, \tag{37}$$

which leads to

$$\square\mathbf{U} \cdot (\square\mathbf{V})^{\dagger} = 0. \tag{38}$$

The vectors $\square\mathbf{U}$ and $(\square\mathbf{V})^{\dagger}$ for the P-wave experiment in Figure 2 are also obtained using equations 21 and 31, $\mathbf{u}_0 = \{1,0,0\}$ and

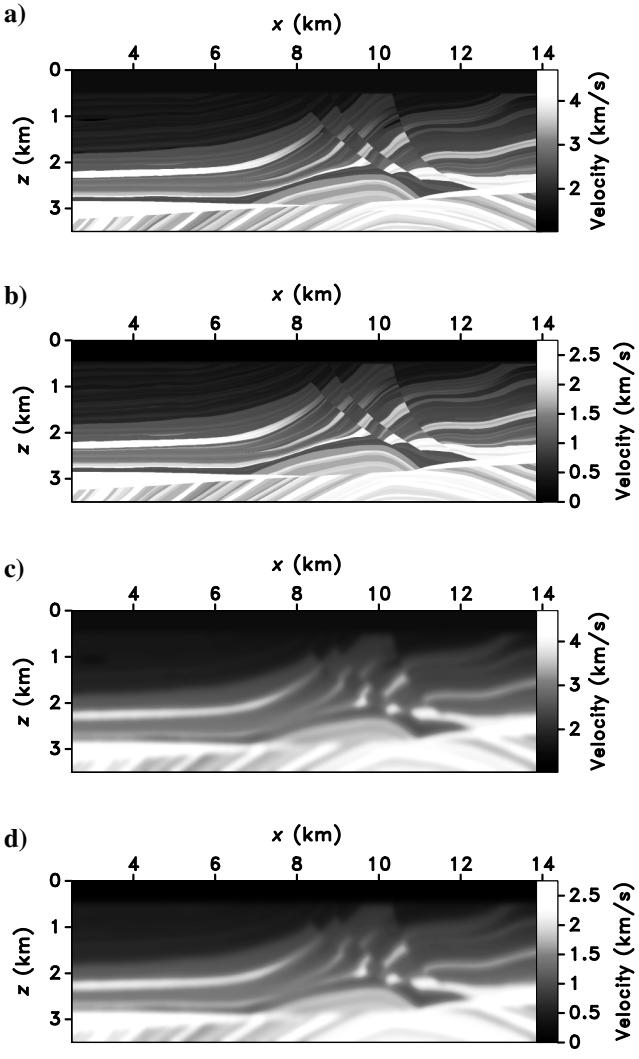


Figure 8. Marmousi-II (a) P- and (b) S-wave velocity. A water layer from $z = 0$ to 0.5 km is present in the model. Panels (c and d) show smoothed versions of (a and b) used for migration, respectively.

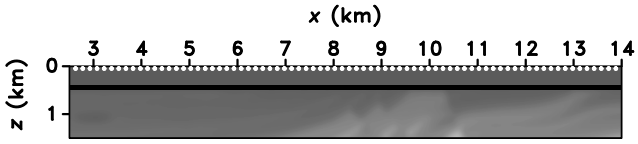


Figure 9. Acquisition geometry used in the Marmousi-II experiment. The white dots indicate the positions of the 76 sources, and the black line at the water bottom indicates a line of receivers.

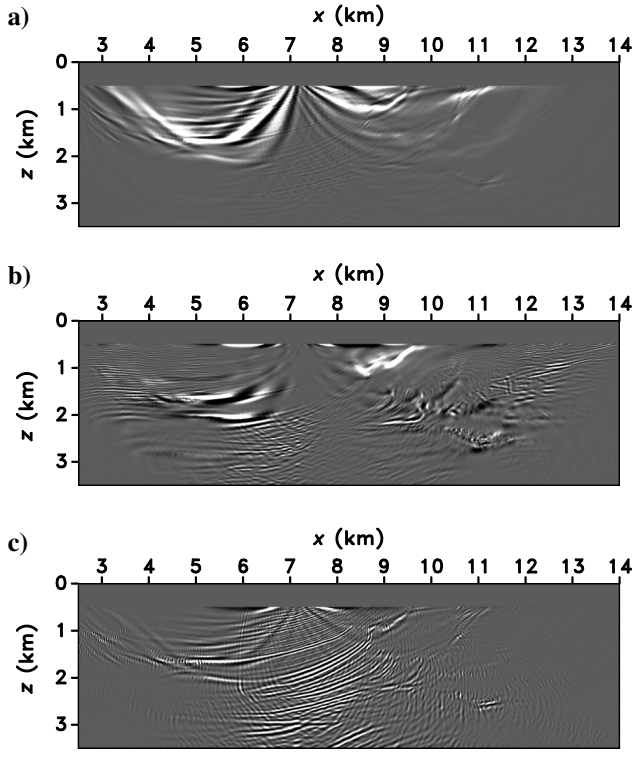


Figure 10. Single-shot images from the Marmousi-II experiment. (a) PP image, (b) SP image, and (c) energy image, which shows no artifacts from polarity reversal and attenuated backscattering energy compared with the conventional images in (a and b).

Downloaded 07/18/16 to 138.67.12.184. Redistribution subject to SEG license or copyright; see Terms of Use at http://library.seg.org/

Downloaded 07/18/16 to 138.67.12.184. Redistribution subject to SEG license or copyright; see Terms of Use at http://library.seg.org/

$\mathbf{p} = \{\sqrt{\rho/(\lambda+2\mu)}, 0, 0\}$:

$$\Box\mathbf{U} = i\omega\sqrt{\rho}\left\{-1, \sqrt{\frac{\lambda+\mu}{\lambda+2\mu}}, \sqrt{\frac{\mu}{\lambda+2\mu}}\right\} e^{i\omega(\mathbf{p}\cdot\mathbf{x}-t)}, \quad (39)$$

$$(\Box\mathbf{V})^{\dagger} = i\omega\sqrt{\rho}\left\{1, \sqrt{\frac{\lambda+\mu}{\lambda+2\mu}}, \sqrt{\frac{\mu}{\lambda+2\mu}}\right\} e^{i\omega(\mathbf{p}\cdot\mathbf{x}-t)}, \quad (40)$$

which also leads to

$$\Box\mathbf{U} \cdot (\Box\mathbf{V})^{\dagger} = 0. \quad (41)$$

EXAMPLES

Using a simple model with a horizontal reflector at $z = 1.5$ km and a vertical displacement source function, we test the proposed imaging condition and compare it with the conventional imaging conditions (Figures 2, 4, and 5). The presence of the reflector in the migration velocity leads to a velocity contrast, causing backscattering artifacts in these numerical experiments. These artifacts appear most prominently in the images using displacement components (Figure 3), PP (Figure 4a), and SS (Figure 4d) images. In the PS (Figure 4b) and SP (Figure 4c) images, the converted reflections do not correlate with the incident waves, thus freeing these images from backscattering artifacts. Note the polarity reversal at normal incidence in Figures 3b, 3c, 4b, and 4c. The energy imaging condition also shows backscattering artifacts (Figure 5c). However, the modified energy imaging condition from equation 35 effectively attenuates the backscattering artifacts (Figure 5d).

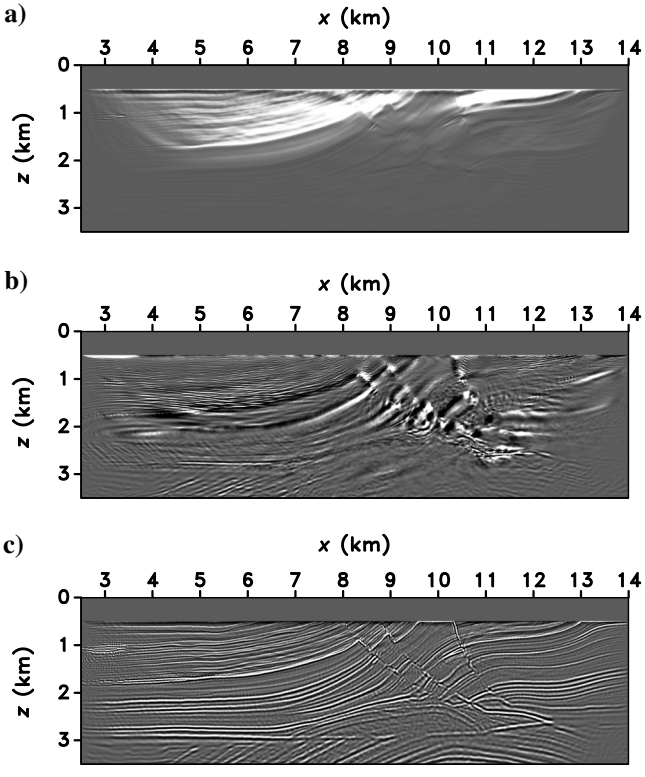


Figure 11. Stacked images from the Marmousi-II experiment. (a) PP image, (b) SP image, and (c) energy image, which shows constructive stacking over shots and attenuated backscattering energy compared with the conventional images in (a and b).

Figures 6 and 7 show a simple 3D elastic experiment, with constant medium parameters and a horizontal reflector. We use a vertical displacement source to generate the source wavefield, and we record the displacement data everywhere at the surface. Similarly to the 2D experiment in Figures 3–5, the images in Figure 6 contain fake mode artifacts (caused by the fact that we do not record the elastic wavefield derivatives at the surface), polarity reversal at normal incidence when correlating different wave modes, and backscattering artifacts when correlating waves propagating along the same path and with the same polarization (the reflector is present at the migration velocity). Figure 7a shows a PP image, and Figure 7b and 7d shows the application of the energy imaging condition: A total energy image (Figure 7b) shows no polarity reversal at normal incidence, but still shows backscattering artifacts; however, the application of the imaging condition in equation 35 forms the image in Figure 7c, with attenuated backscattering artifacts compared with Figure 7b. Although the fake mode artifacts are present in Figure 7c, stacking over a considerable number of shots attenuates this type of artifacts, as shown in Figure 7d.

Figures 8a, 8b and 9 show the Marmousi-II (Martin et al., 2002) model parameters and acquisition geometry used to model synthetic data and for testing our new elastic imaging condition. The synthetic data are acquired at a horizontal line of displacement sensors located at the water bottom ($z = 0.50$ km); the 76 pressure sources are located near the surface of the water layer ($z = 0.05$ km) and horizontally spaced from each other by 150 m. This acquisition geometry resembles an ocean-bottom seismic (OBS) survey, recording multicomponent data at the water bottom (Figure 9). The P and S migration velocities (Figure 8c and 8d) are smoothed versions of the stratigraphic velocities used to model the synthetic data to reduce the artifacts at places with a high velocity gradient. Using the conventional imaging conditions for the PP- and SP-wave modes, we obtain the images in Figure 10a and 10b for shot number 30, and the images in Figure 11a and 11b after stacking over all shots in this simulated survey. Artifacts due to diving waves and some residual backscattering created by the heterogeneities from the model are present in both conventional images. Figure 11b also shows the effects of nonconstructive stacking due to polarity reversal seen, for example, in the single-shot image shown in Figure 10b. We attenuate all these artifacts in Figure 11c using the energy imaging condition from equation 35. Similar to the 3D experiment in Figure 7c and 7d, the individual elastic images for single shots (Figure 10c) have only fake mode artifacts, which are attenuated after stacking over shots, leading to a good-quality image, as shown in Figure 11c.

CONCLUSIONS

The energy imaging condition offers an alternative to the conventional imaging conditions, which use potentials or displacement components. This alternative combines all wave modes into a single image and does not suffer from polarity reversal, as is the case for conventional images using converted modes, either with potentials or displacements. The energy imaging condition accounts for wavefield directionality, including the wavefield propagation and polarization directions. We describe this imaging condition as the projection between the multidimensional vectors $\Box\mathbf{U}$ and $\Box\mathbf{V}$ (built

Downloaded 07/18/16 to 138.67.12.184. Redistribution subject to SEG license or copyright; see Terms of Use at http://library.seg.org/

using the extrapolated wavefields **U** and **V**), whose terms contain information about wavefield directionality. By exploiting this directionality, we are able to attenuate the backscattering artifacts in the imaging, in a way that is similar to the case with acoustic waves. The elastic energy image is scalar, like an acoustic image. However, in contrast with its acoustic counterpart, the elastic energy image retains all the benefits of elastic imaging: (1) injection of multicomponent data without wave-mode decomposition, which is not feasible with conventional OBS data, (2) increased subsurface illumination from converted waves in the presence of complex structures, and (3) amplitude behavior that accounts for S-wave properties.

ACKNOWLEDGMENTS

We would like to thank the sponsor companies of the Consortium Project on Seismic Inverse Methods for Complex Structures, whose support made this research possible. We acknowledge Y. Duan, who provided the elastic modeling code for this research. The reproducible numeric examples in this paper use the Madagascar open-source software package (Fomel et al. 2013) freely available from http://www.ahay.org.

APPENDIX A

CONSERVATION OF ENERGY FOR AN ACOUSTIC WAVEFIELD

Given a solution to the acoustic-wave equation:

$$\ddot{U} - c^2\nabla^2 U = 0, \tag{A-1}$$

we can define the energy at time t (Evans, 1997; McOwen, 2003) as

$$E(t) = \frac{1}{2}\int_{\mathbb{R}^N} (\dot{U}^2 + c^2|\nabla U|^2)d\mathbf{x}. \tag{A-2}$$

The energy gives an integral measure of the regularity of U for the first-order derivation.

Let us define the domain in which the solution is valid by $\Omega \in \mathbb{R}^N$. Considering c is a finite propagation speed, one can assume U and its derivatives are close to zero on the boundary $\partial\Omega$ for all times if Ω is sufficiently large. The conservation of energy means $\dot{E}(t) = 0$; therefore, differentiating $E(t)$ within the domain Ω yields

$$\dot{E}(t) = \int_\Omega (\dot{U}\ddot{U} + c^2\nabla U \cdot \nabla\dot{U})d\mathbf{x}. \tag{A-3}$$

The second term in the integrand can be integrated by parts:

$$\int_\Omega c^2(\nabla U \cdot \nabla\dot{U})dx = \int_\Omega c^2\nabla\cdot(\dot{U}\nabla U)dx - \int_\Omega c^2(\dot{U}\nabla^2 U)d\mathbf{x}. \tag{A-4}$$

The first term of the right side can be turned into a surface integral by the divergence theorem, and then it goes to zero because U and its derivatives vanish on the boundary $\partial\Omega$. Substituting the remaining term in equation A-3 yields

$$\dot{E}(t) = \int_\Omega \dot{U}(\ddot{U} - c^2\nabla^2 U)d\mathbf{x} = 0, \tag{A-5}$$

because the wavefield u satisfies the wave equation in equation A-1.

The energy norm for an acoustic wavefield can be considered as a special case of the isotropic energy norm. Using vector calculus identities, equation 18 can be rewritten as

$$\rho\ddot{\mathbf{U}} = (\lambda + 2\mu)[\nabla(\nabla\cdot\mathbf{U})] - \mu[\nabla\times(\nabla\times\mathbf{U})]. \tag{A-6}$$

If the particle displacement **U** is has only compressional behavior, the term $[\nabla\times(\nabla\times\mathbf{U})]$ is zero.

Equation A-6 becomes

$$\rho\ddot{\mathbf{U}} = (\lambda + 2\mu)[\nabla(\nabla\cdot\mathbf{U})]. \tag{A-7}$$

The energy norm for this wave equation is

$$E(t) = \frac{1}{2}\int_\Omega \rho\|\dot{\mathbf{U}}\|^2 + (\lambda + 2\mu)\|\nabla\cdot\mathbf{U}\|^2 d\mathbf{x}. \tag{A-8}$$

In this form, the energy norm refers to the particle displacement **U**. In a more general sense, this norm applies for any wavefield. We know that the particle velocity **S** is only 90° out of phase from **U**. Therefore,

$$E(t) = \frac{1}{2}\int_\Omega \rho\|\dot{\mathbf{S}}\|^2 + (\lambda + 2\mu)\|\nabla\cdot\mathbf{S}\|^2 d\mathbf{x}. \tag{A-9}$$

This can also be explained by deriving equation A-8 in time, obtaining equation A-9. The equations that relate particle velocity and pressure from continuum mechanics are (Webster, 2000)

$$\rho\dot{\mathbf{S}} = -\nabla p, \tag{A-10}$$

$$\nabla\cdot\mathbf{S} = -\frac{1}{(\lambda + 2\mu)}\dot{p}. \tag{A-11}$$

Rewriting the two equations above in terms of the norms:

$$\rho^2\|\dot{\mathbf{S}}\|^2 = -\|\nabla p\|^2, \tag{A-12}$$

$$\|\nabla\cdot\mathbf{S}\|^2 = -\frac{1}{(\lambda + 2\mu)^2}\|\dot{p}\|^2. \tag{A-13}$$

Substituting these last expressions in equation A-9, we obtain

$$E(t) = -\frac{1}{2}\int_\Omega \frac{\|\nabla p\|^2}{\rho} + \frac{1}{(\lambda + 2\mu)}\|\dot{p}\|^2 d\mathbf{x}. \tag{A-14}$$

Scaling this energy measure by $\rho(\lambda + 2\mu)$:

$$E(t) = -\frac{1}{2}\int_\Omega \rho\|\dot{p}\|^2 + (\lambda + 2\mu)\|\nabla p\|^2 d\mathbf{x}, \tag{A-15}$$

which is equivalent to equation A-2, considering U as the scalar pressure field, and $c = \sqrt{(\lambda + 2\mu)/\rho}$.

Downloaded 07/18/16 to 138.67.12.184. Redistribution subject to SEG license or copyright; see Terms of Use at http://library.seg.org/

APPENDIX B

FROBENIUS PRODUCT AND NORM

The Frobenius norm is the most common matrix norm in numerical linear algebra. Consider an arbitrary matrix $A_{M\times N}$, this norm is defined as (Golub and Loan, 1996)

$$\|A\|_F = \sqrt{\sum_{i=1}^{M}\sum_{j=1}^{N}|a_{ij}|^2}. \tag{B-1}$$

We can also define the norm based on the inner product of associate matrices. Given matrices A and B, we can define the Frobenius product,

$$\langle A, B\rangle_F = A:B = \sum_{i=1}^{M}\sum_{j=1}^{N} a_{ij}b_{ij}, \tag{B-2}$$

where A and B are of dimension $M\times N$. This product can also be written in matrix form as

$$\langle A, B\rangle_F = A:B = \mathrm{Tr}(A^{\mathrm{T}}B) = \mathrm{Tr}(AB^{\mathrm{T}}). \tag{B-3}$$

Then, we can write the Frobenius norm:

$$\|A\|_F = \sqrt{\mathrm{Tr}(AA^{\mathrm{T}})}. \tag{B-4}$$

APPENDIX C

STRAIN ENERGY FUNCTION IN ISOTROPIC MEDIA

In a general elastic medium subject to infinitesimal strains, the strain energy function is (Slawinski, 2003)

$$E(\epsilon) = \frac{1}{2}c_{ijlk}\epsilon_{kl}\epsilon_{ij}, \tag{C-1}$$

where c_{ijlk} is an element of the stiffness tensor $\mathbf{c}$ and ϵ_{ij} is an element of the strain tensor $\mathbf{e}$. The repeated indices i, j, k, l imply summation, following the Einstein convention. For an isotropic medium, the stiffness coefficients are (Aki and Richards, 2002)

$$c_{ijlk} = \lambda\delta_{ij}\delta_{kl} + \mu\delta_{ik}\delta_{jl} + \mu\delta_{il}\delta_{jk}, \tag{C-2}$$

where δ_{ij} is the Kronecker delta function and λ and μ are the Lamé parameters. Substituting equation C-2 in equation C-1, we obtain

$$E(\epsilon) = \frac{1}{2}[\lambda\delta_{ij}\delta_{kl} + \mu\delta_{ik}\delta_{jl} + \mu\delta_{il}\delta_{jk}]\epsilon_{kl}\epsilon_{ij}. \tag{C-3}$$

Considering the Kronecker delta function is equal to unity for equal indices and zero otherwise, we develop each term and obtain

$$E(\epsilon) = \frac{1}{2}[\lambda\epsilon_{ii}\epsilon_{kk} + \mu\epsilon_{ij}\epsilon_{ij} + \mu\epsilon_{ji}\epsilon_{ij}]. \tag{C-4}$$

These implicit summations can be written in matrix form as

$$E(\underline{\mathbf{e}}) = \frac{1}{2}[\lambda\mathrm{Tr}[\underline{\mathbf{e}}]\mathrm{Tr}[\underline{\mathbf{e}}] + \mu(\underline{\mathbf{e}}:\underline{\mathbf{e}}) + \mu(\underline{\mathbf{e}}:\underline{\mathbf{e}}^{\mathrm{T}})]. \tag{C-5}$$

As the strain tensor is symmetric, we obtain

$$E(\underline{\mathbf{e}}) = \frac{1}{2}[\lambda(\mathrm{Tr}[\underline{\mathbf{e}}])^2 + 2\mu(\underline{\mathbf{e}}:\underline{\mathbf{e}})]. \tag{C-6}$$

The strain tensor $\underline{\mathbf{e}}$ is a function of the wavefield derivatives

$$\underline{\mathbf{e}} = \frac{1}{2}[\nabla\mathbf{U} + \nabla\mathbf{U}^{\mathrm{T}}]. \tag{C-7}$$

Substituting, we have

$$\begin{aligned} E(\underline{\mathbf{e}}) &= \frac{1}{2}\left[\lambda\|\nabla\cdot\mathbf{U}\|^2 + 2\mu\left(\frac{1}{2}(\nabla\mathbf{U} + \nabla\mathbf{U}^{\mathrm{T}}):\frac{1}{2}(\nabla\mathbf{U} + \nabla\mathbf{U}^{\mathrm{T}})\right)\right], \\ &= \frac{1}{2}\left[\lambda\|\nabla\cdot\mathbf{U}\|^2 + \frac{1}{2}\mu(\nabla\mathbf{U}:\nabla\mathbf{U} + 2\nabla\mathbf{U}:\nabla\mathbf{U}^{\mathrm{T}} + \nabla\mathbf{U}^{\mathrm{T}}:\nabla\mathbf{U}^{\mathrm{T}})\right], \\ &= \frac{1}{2}[\lambda\|\nabla\cdot\mathbf{U}\|^2 + \mu(\nabla\mathbf{U}:\nabla\mathbf{U} + \nabla\mathbf{U}:\nabla\mathbf{U}^{\mathrm{T}})], \end{aligned} \tag{C-8}$$

which corresponds to the potential energy terms of equation 15.

APPENDIX D

TERMS NOT ACCOUNTABLE FOR THE TOTAL ENERGY

Integrating the strain energy function for the isotropic case (equation C-8) over the whole spatial domain:

$$E_{\mathbf{e}} = \frac{1}{2}\int_{\Omega}\lambda\|\nabla\cdot\mathbf{U}\|^2 + \mu(\nabla\mathbf{U}:\nabla\mathbf{U} + \nabla\mathbf{U}:\nabla\mathbf{U}^{\mathrm{T}})d\mathbf{x}, \tag{D-1}$$

where the gradient of the displacement vector consists of the following elements:

$$\nabla\mathbf{U} = \frac{\partial U_i}{\partial x_j} = \begin{bmatrix} U_{1,1} & U_{1,2} & U_{1,3} \\ U_{2,1} & U_{2,2} & U_{2,3} \\ U_{3,1} & U_{3,2} & U_{3,3} \end{bmatrix}. \tag{D-2}$$

Rewriting equation D-1 in terms of these elements, we get

$$\begin{aligned} E_{\mathbf{e}} &= \frac{1}{2}\int_{\Omega}\lambda\|\nabla\cdot\mathbf{U}\|^2 + \mu(\nabla\mathbf{U}:\nabla\mathbf{U} + U_{i,i}^2 + 2U_{2,1}U_{1,2} \\ &\quad + 2U_{2,3}U_{3,2} + 2U_{1,3}U_{3,1})d\mathbf{x}, \\ &= \frac{1}{2}\int_{\Omega}\lambda\|\nabla\cdot\mathbf{U}\|^2 + \mu(\nabla\mathbf{U}:\nabla\mathbf{U}) + \mu(U_{i,i})^2 \\ &\quad + \mu(U_{i,j}U_{j,i} - U_{i,i}U_{j,j})d\mathbf{x}, \\ &= \frac{1}{2}\int_{\Omega}(\lambda+\mu)\|\nabla\cdot\mathbf{U}\|^2 + \mu(\nabla\mathbf{U}:\nabla\mathbf{U}) \\ &\quad + \mu(U_{i,j}U_{j,i} - U_{i,i}U_{j,j})d\mathbf{x}. \end{aligned} \tag{D-3}$$

The terms $(U_{i,j}U_{j,i} - U_{i,i}U_{j,j})$ integrated over the whole spatial domain become zero. We can show it by an example with x and y, with $\mathbf{U} = \{u, v, w\}$:

$$\iint \left(\frac{\partial u}{\partial y}\frac{\partial v}{\partial x} - \frac{\partial u}{\partial x}\frac{\partial v}{\partial y}\right) dxdy. \tag{D-4}$$

Integrating by parts the second term of the integrand, and assuming u and v vanish at the boundaries, we have

$$\iint \left(\frac{\partial u}{\partial y}\frac{\partial v}{\partial x} + u\frac{\partial^2 v}{\partial x \partial y}\right) dxdy. \tag{D-5}$$

Integrating the second term by parts once more, and assuming u and v have the second-order continuous derivatives, we have

$$\iint \left(\frac{\partial u}{\partial y}\frac{\partial v}{\partial x} - \frac{\partial u}{\partial y}\frac{\partial v}{\partial x}\right) dxdy = 0, \tag{D-6}$$

which makes the total energy in equations 15 and 17 equivalent when the second-order derivatives are continuous.

APPENDIX E

ELASTIC-WAVE EQUATION AND CONTINUITY OF SECOND-ORDER DERIVATIVES

Equation 2 has the following wave equation:

$$\rho\ddot{\mathbf{U}} = \lambda[\nabla(\nabla \cdot \mathbf{U})] + \mu[\nabla \cdot (\nabla\mathbf{U} + \nabla\mathbf{U}^{\mathrm{T}})], \tag{E-1}$$

which can be simplified further when using the following calculus identity:

$$[\nabla \cdot (\nabla\mathbf{U} + \nabla\mathbf{U}^{\mathrm{T}})] = \nabla(\nabla \cdot \mathbf{U}) + \nabla^2\mathbf{U}. \tag{E-2}$$

In index form, this identity is

$$U_{j,ij} + U_{i,jj} = U_{j,ji} + U_{i,jj}. \tag{E-3}$$

Notice that, for this identity to be valid, second-order derivatives must be continuous, so we can interchange derivatives for $U_{j,ij} = U_{j,ji}$. Therefore, assuming this identity to be true, equation E-1 becomes

$$\rho\ddot{\mathbf{U}} = (\lambda + \mu)\nabla(\nabla \cdot \mathbf{U}) + \mu\nabla^2\mathbf{U}. \tag{E-4}$$

APPENDIX F

CHRISTOFFEL EQUATION FOR ISOTROPIC MEDIA

The Christoffel equation for anisotropic media is (Musgrave, 1970; Tsvankin, 2012)

$$[c_{ijkl}p_j p_l - \rho\delta_{ik}]u_k = 0, \tag{F-1}$$

where δ_{ij} is the Kronecker delta function, c_{ijkl} is the stiffness tensor, $\rho(\mathbf{x})$ is the density, u_k is the kth component of the polarization vector $\mathbf{u}_0$, and p_j and p_l are the jth and lth components of the slowness vector $\mathbf{p}$. We can rewrite equation F-1 as

$$\rho u_i = u_k c_{ijkl} p_j p_l. \tag{F-2}$$

The stiffness coefficients for isotropic media are defined by

$$c_{ijlk} = \lambda\delta_{ij}\delta_{kl} + \mu\delta_{ik}\delta_{jl} + \mu\delta_{il}\delta_{jk}, \tag{F-3}$$

where $\lambda(\mathbf{x})$ and $\mu(\mathbf{x})$ are the Lamé parameters. Substituting the isotropic stiffness definition in equation F-2, we obtain

$$\rho u_i = u_k(\lambda\delta_{ij}\delta_{kl} + \mu\delta_{ik}\delta_{jl} + \mu\delta_{il}\delta_{jk})p_j p_l, \tag{F-4}$$

$$= u_k(\lambda p_i p_k + \mu\delta_{ik}p_j p_j + \mu p_i p_k), \tag{F-5}$$

$$= (\lambda + \mu)(u_k p_k)p_i + \mu(p_j p_j)u_i, \tag{F-6}$$

with summation over indices k and j. We can rewrite equation F-6 in vector form as

$$\rho\mathbf{u}_0 = (\lambda + \mu)(\mathbf{u}_0 \cdot \mathbf{p})\mathbf{p} + \mu(\mathbf{p} \cdot \mathbf{p})\mathbf{u}_0. \tag{F-7}$$

Finally, we can also rewrite the Christoffel equation in equation F-7 in terms of P and S velocities

$$\mathbf{u}_0 = (V_{\mathrm{P}}^2 - V_{\mathrm{S}}^2)(\mathbf{u}_0 \cdot \mathbf{p})\mathbf{p} + V_{\mathrm{S}}^2(\mathbf{p} \cdot \mathbf{p})\mathbf{u}_0. \tag{F-8}$$

REFERENCES

Aki, K., and P. G. Richards, 2002, Quantitative seismology (2nd ed.): University Science Books.

Balch, A. H., and C. Erdermir, 1994, Sign-change correction for prestack migration of P-S converted wave reflections: Geophysical Prospecting, **42**, 637–663, doi: 10.1111/gpr.1994.42.issue-6.

Boas, M. L., 2006, Vector analysis, *in* Mathematical Methods in the Physical Sciences, 3rd ed.: John Wiley & Sons, 318–320.

Chang, W.-F., and G. A. McMechan, 1987, Elastic reverse-time migration: Geophysics, **52**, 1365–1375, doi: 10.1190/1.1442249.

Chen, T., and L. Huang, 2014, Elastic reverse-time migration with an excitation amplitude imaging condition: 84th Annual International Meeting, SEG, Expanded Abstracts, 1868–1872.

Claerbout, J. F., 1971, Toward a unified theory of reflector mapping: Geophysics, **36**, 467–481, doi: 10.1190/1.1440185.

Dellinger, J., and J. Etgen, 1990, Wave-field separation in two-dimensional anisotropic media: Geophysics, **55**, 914–919, doi: 10.1190/1.1442906.

Denli, H., and L. Huang, 2008, Elastic-wave reverse-time migration with a wavefield-separation imaging condition: 78th Annual International Meeting, SEG, Expanded Abstracts, 2346–2350.

Duan, Y., and P. Sava, 2014a, Converted-waves imaging condition for elastic reverse-time migration: 84th Annual International Meeting, SEG, Expanded Abstracts, 1904–1908.

Duan, Y., and P. Sava, 2014b, Elastic reverse-time migration with OBS multiples: 84th Annual International Meeting, SEG, Expanded Abstracts, 4071–4076.

Etgen, J. T., 1988, Prestacked migration of P- and SV-waves: 58th Annual International Meeting, SEG, Expanded Abstracts, 972–975.

Evans, L. C., 1997, Partial differential equations: American Mathematical Society 19.

Fomel, S., P. Sava, I. Vlad, Y. Liu, and V. Bashkardin, 2013, Madagascar: Open-source software project for multidimensional data analysis and reproducible computational experiments: Journal of Open Research Software, **1**, doi: 10.5334/jors.ag.

Golub, G. H., and C. F. V. Loan, 1996, Chapter 2 — Matrix analysis, in matrix computations (3 ed.): John Hopkins University Press.

Guitton, A., B. Kaelin, and B. Biondi, 2007, Least-squares attenuation of reverse-time-migration artifacts: Geophysics, **72**, no. 1, S19–S23, doi: 10.1190/1.2399367.

Hokstad, K., R. Mittet, and M. Landrø, 1998, Elastic reverse time migration of marine walkaway vertical seismic profiling data: Geophysics, **63**, 1685–1695, doi: 10.1190/1.1444464.

Martin, G., K. Marfurt, and S. Larsen, 2002, Marmousi-2, an updated model for the investigation of AVO in structurally complex areas: 72nd Annual International Meeting, SEG, Expanded Abstracts, 1979–1982.

McOwen, R. C., 2003, Partial differential equations: Methods and applications (2 ed.): Prentice Hall.

Musgrave, M., 1970, Crystal acoustics: Holden-Day.

Downloaded 07/18/16 to 138.67.12.184. Redistribution subject to SEG license or copyright; see Terms of Use at http://library.seg.org/

Ravasi, M., and A. Curtis, 2013, Elastic imaging with exact wavefield extrapolation for application to ocean-bottom 4C seismic data: Geophysics, **78**, no. 6, S265–S284, doi: 10.1190/geo2013-0152.1.
Rocha, D., N. Tanushev, and P. Sava, 2015, Acoustic wavefield imaging using the energy norm: 85th Annual International Meeting, SEG, Expanded Abstracts, 4085–4090.
Slawinski, M. A., 2003, Seismic waves and rays in elastic media (1 ed.): Elsevier Science 34.
Tsvankin, I., 2012, Seismic signatures and analysis of reflection data in anisotropic media (3 ed.): SEG.
Webster, J., 2000, Chapter 8.1 — The wave equation, in mechanical variables measurement: Solid, fluid and thermal (1 ed.): CRC Press.
Yan, J., and P. Sava, 2007, Elastic wavefield imaging with scalar and vector potentials: 77th Annual International Meeting, SEG, Expanded Abstracts, 2150–2154.
Yan, J., and P. Sava, 2008, Isotropic angle-domain elastic reverse-time migration: Geophysics, **73**, no. 6, S229–S239, doi: 10.1190/1.2981241.
Yan, J., and P. Sava, 2009, Elastic wave-mode separation for VTI media: Geophysics, **74**, no. 5, WB19–WB32, doi: 10.1190/1.3184014.
Yan, J., and P. Sava, 2011, Improving the efficiency of elastic wave-mode separation for heterogeneous TTI media: Geophysics, **76**, no. 4, T65–T78, doi: 10.1190/1.3581360.
Yan, R., and X.-B. Xie, 2010, The new angle-domain imaging condition for elastic RTM: 80th Annual International Meeting, SEG, Expanded Abstracts, 3181–3186.
Yan, R., and X.-B. Xie, 2012, An angle-domain imaging condition for elastic reverse time migration and its application to angle gather extraction: Geophysics, **77**, no. 5, S105–S115, doi: 10.1190/geo2011-0455.1.
Yoon, K., and K. J. Marfurt, 2006, Reverse-time migration using the Poynting vector: Exploration Geophysics, **37**, 102–107, doi: 10.1071/EG06102.
Youn, O., and H. W. Zhou, 2001, Depth imaging with multiples: Geophysics, **66**, 246–255, doi: 10.1190/1.1444901.
Zhe, J., and S. A. Greenhalg, 1997, Prestack multicomponent migration: Geophysics, **62**, 598–613, doi: 10.1190/1.1444169.

Downloaded 07/18/16 to 138.67.12.184. Redistribution subject to SEG license or copyright; see Terms of Use at http://library.seg.org/